Comparison of ionic liquid electrolyte to aqueous electrolytes on carbon nanofibres supercapacitor electrode derived from oxygen-functionalized graphene

Kabir O. Oyedotun[1], Tshifhiwa M. Masikhwa[1], Simon Lindberg[2], Aleksandar Matic[2], Patrik Johansson[2], and Ncholu Manyala[1]*

[1]Department of Physics, Institute of Applied Materials, SARChI Chair in Carbon Technology and Materials, University of Pretoria, Pretoria 0002, South Africa.
[2]Department of Physics, Chalmers University of Technology, 41296 Gothenburg, Sweden.

*Corresponding author's email: ncholu.manyala@up.ac.za, Tel.: + (27)12 420 3549.

Highlights

- Novel RGO-derived carbon nanofibres material is synthesized.
- The synthesized material is examined as supercapacitors electrodes using various electrolytes.
- A fabricated symmetric device exhibits higher energy density and superior stability in ILE.
- The device's unique stability in ILE displays its efficacy as electrode for energy storage applications.

Abstract

A facial force-driven reflux technique was used to develop fibre-like carbon material from freeze-dried reduced graphene oxide (RGO) firstly prepared by using a modified Hummers method. The carbon nanofibres displayed a high specific surface area of ~ 1317.8 m^2g^{-1}, with good pore size distributions which could be beneficial for energy storage applications. Electrochemical measurements of the carbon nanofibre electrodes in a symmetric configuration with aqueous (1 M Na_2SO_4, 6 M KOH), and protic ionic liquid (1-ethylimidazolium bis(trifluoromethanesulfonly)imide) electrolytes (ILE) displayed excellent electrochemical performance with the dominant electric double layer capacitor (EDLC) behaviour. The fabricated

device shows higher electrochemical performance in the ILE due to its larger cell operating potential (3.0 V) as compared with the aqueous electrolytes (0.8 V). The optimized electrochemical properties especially in terms of higher specific energy and superior stability, suggest the material's potential applications as electrode for supercapacitors.

Graphical abstract

Keywords: Ionic liquid electrolyte (ILE); specific surface area (SSA); graphene; specific energy; nanofibres; reflux technique.

Introduction

The intense study to developing high specific energy capacitors with a focus on rational designing of nanoscale electrode materials with a view to reducing their electron-ion diffusion length for ultrafast charge-discharge performance. Thus, an optimal electrode design constituting a sinewy 3-dimensional interconnecting structure couple with high specific surface area and short ion/electron diffusion length is of paramount importance [1,2].

Supercapacitor, SC also referred to as electrochemical capacitor or ultracpacitor is a device with much higher capacitance but lower potential limits than the conventional capacitors. It bridges the gap between the conventional capacitors and rechargeable batteries such as lithium ion batteries. SC exhibits more specific energy than the conventional capacitors. It can accept and deliver charges much faster, and tolerate many more charge and discharge cycles than rechargeable batteries [3,4].

The performance and cost of commercial SCs is greatly influenced by the choice of electrode materials. The electrode material significantly determines the device's specific energy, since it characteristically has a higher specific power than the rechargeable batteries. Thus, the active element of the electrodes is the key, and dictates how best a commercial SC performs [3,5].

Graphene, which is essentially a form of carbon, has attracted more attentions among researchers than the popular and extremely high relative surface area activated carbon [6]. Graphene has been reported several times as a promising candidate for electrode materials due to its ability to facilitate electron or hole transfer along its two-dimensional surface [6,7]. Researches have indicated that graphene sheets are desirable candidates for enhancing the performance of electrode materials for electrochemical capacitors to match the demands of consumers. The impedance analysis of some of the graphene-based composites suggested their charge transfer resistance to be very low, which accounts for their excellent rate capability [7,8].

Graphene offers many advantages over using typical electrochemical capacitor electrode materials in a standalone fashion. First, the graphene can serve as a binder material, eliminating the use of binding polymer materials such as poly vinylidene fluoride (PVDF) [8]. Second, the high conductivity associated with graphene sheets lends itself to rapid transport of ions to and from the active material insertion sites, particularly given the close physical association of the nanoparticles and the reduced graphene oxide (RGO) sheets [9]. Also the mechanical strength of

the graphene has the potential to absorb some of the expansion and contraction of the anchored nanoparticles during charge and discharge processes [10]. These typically lead to mechanical failure of the electrode and performance reduction through the loss of intimate contact of the active material and the conductive carbon black mixed into the electrode material for enhanced conductivity. The electrode can ultimately be pulverized if the expansion is large enough, hence the use of active materials that exhibit small changes upon ion insertion [9,10].

In spite of the excellent properties of graphene such as superb chemical and thermal stability, excellent electrical properties, high specific surface area (SSA) (about 2630 m^2 g^{-1}) and good flexibility among others, graphene-based electrode materials are still plagued with low specific energies when employed in energy storage devices such as supercapacitors. Graphene oxide (GO) has been broadly prepared by using the oxidation of graphite powder, with prevalent study been done to unravel its chemical structure and/or surface chemistry [8,11].

The performance of the material (GO) can be largely improved by modifying its surface chemistry such as by optimizing the oxygen-containing surface functionalities, as well as the morphological properties. Apart from modifying the electrode material, specific energy of a supercapacitor can be improved by increasing the operating potential through the adoption of other electrolytes with larger potential window such as ionic liquids electrolytes.

This work has reported on the role of electrolyte and morphology control for improving the specific energy of graphene-based supercapacitor electrodes. The RGO derived carbon nanofibre electrode material with length of about tens of microns was synthesized for the first time via a novel, simple and cost-effective constant stirring reflux method. The method provides a homogeneous blend of reactants thereby, speeding up reaction rates whist preserving constant reaction conditions such as volume, concentration, atmospheric pressure and temperature.

Experimental

Synthesis of sheet-like reduced graphene oxide and carbon nanofibres

The sheet-like reduced graphene oxide (RGO) was synthesized via a modified Hummers method by adding graphite powder and $KMnO_4$ together with a certain volume of concentrated sulphuric acid (H_2SO_4), and subsequent addition of 30% H_2O_2 and DI water to obtain the final sample *(See supporting information for details about synthesis procedure and also reference* [12]*).*

The carbon nanofibres material was synthesized by re-dispersing 3.0 g of sheet-like RGO into a highly concentrated aqueous NaOH solution (40 wt.%, 450 ml) upon constant stirring (600 revolutions per minute (rpm)) in a reflux set-up inserted in silicone oil bath to ensure even reaction temperature of 130 °C throughout the process. The choice of 130 °C as reaction temperature is based on the boiling point (between 120 – 140 °C) of the high concentration NaOH solution. The synthesis carried out under the reflux system was adopted to ensure that the pressure within the system during synthesis is maintained at atmospheric pressure. The process was allowed to dwell for 24 h. After cooling to room temperature, the recovered mixture was dispersed in 3 M HCl (200 mL) to adjust its pH, and then centrifuged for 10 min. at 10000 rpm. The recovered solid sample was dry overnight at 60 °C in ambient condition using an electric oven, and was later annealed in air at 100 °C at a ramping rate of 1 °C/min. for 2h to thermally dehydrate and deoxygenate the obtained raw carbon nanofibres material.

Sample characterization

The as-synthesized material's morphology and micrograph were observed with the aid of a Zeiss Ultra Plus 55 field emission scanning electron microscope (FE-SEM) at 2.0 KV operating potential, and a JEOL-2100F transmission electron microscope (TEM FEI Technai-F30)

operating at an acceleration voltage of 200 kV. A Bruker BV 2D PHASER Best Benchtop X-ray diffraction (XRD) analyzer with reflection geometry at 2θ values (10–90°) with a step size of 0.005 °, operating with a Cu $K\alpha_1$ radiation source (λ = 0.15406 nm) at 50 kV and 30 mA was employed to study the material's phase structure. X-ray photoelectron spectroscopy (XPS) analyzer (Versa Probe 5000 spectrometer activated with a 100 μm monochromatic Al-Kα exciting source) was utilized to characterize the electronic states of surface elements in the material. Nitrogen adsorption–desorption isotherms were measured using a Micromeritics TriStar II 3020 analyzer incorporated with the Brunauer-Emmett-Teller (BET) and Barrett–Joyner–Halenda (BJH) models to determine the specific surface area pore size distribution respectively. Raman analysis was obtained through a WITec alpha 300 RAS+ Confocal Raman microscope (Focus Innovations, Germany) set on the 532 nm laser wavelength with a spectral acquisition time and laser power of 150 s and 5 mW respectively.

Electrode fabrication and electrochemical measurements

The sample electrodes were fabricated by coating the slurry formed from dissolution of 80 wt% active material, 10 wt.% carbon black, and 10 wt.% polyvinylidenedifluoride (PVDF) in small amount of N-methylpyrrolidone (NMP) on circular nickel foam current collector, and subsequently dried at 70 °C overnight. The actual total loading masses of the electrodes in the symmetric device in different electrolytes were determined to be ~ 5.26 mg (1 M Na_2SO_4), ~ 5.31 mg (6 M KOH), and ~ 5.25 mg (ILE) respectively, with each electrode having an area of about 1.77×10^{-4} m^2. The SC devices were assembled using a standard 2032 grade coin cells with a Watman Celgard paper-based separator, and 1 M Na_2SO_4, 6 M KOH as well as 1-ethylimidazolium bis(trifluoromethanesulfonly)imide (ILE) used as electrolytes, respectively. Device fabrication for the ILE was performed in an argon-filled glove box with sub-0.9 ppm water and 0.1 ppm oxygen contents. Cycling voltammetry (CV), Galvanostatic charge-discharge

(GCD), and electrochemical impedance spectroscopy (EIS) measurements were performed by adopting a Bio-Logic VMP300 potentiostat (Knoxville TN 37,930, USA) controlled by the EC-Lab® V1.40 software.

The specific capacitance, C_{sp} ($F\ g^{-1}$) for single electrode of the symmetric device with respect to specific current of the device was extracted through the slope of the charge-discharge profile in line with equation 1 below [13,14]:

$$C_{sp} = \frac{4I}{m \times \frac{\Delta V}{\Delta t}} \quad (1)$$

where I is the applied current (A), m is total mass (g) of active material, and $\frac{\Delta V}{\Delta t}$ represents slope extracted from the discharge curve. Thus, the values of capacitance presented in this work are expressed per mass of each electrode.

Energy density (E_d) expressed in Wh kg^{-1} and the corresponding power density (P_d) in kw kg^{-1} of the device were deduced via relations 2 and 3, respectively [13]:

$$E_d = \frac{\mathrm{C} \cdot \Delta V^2}{28.8} \quad (2)$$

$$P_d = 3.6 \times E_d/\Delta t \quad (3)$$

where ΔV and Δt are cell operating potential (volts) and discharge time (s), respectively.

Results and discussion

Formation mechanism of the carbon nanofibres

In a characteristic synthesis, high concentration of NaOH aqueous solution (10 M; 40 wt. %) was selected as a based-fluid for the transformation of the nanosheets into fibre-like materials. The whole formation mechanism of the carbon nanofibres is based on the diffusion rates and a

chemical reaction taking place between high concentration of NaOH solution and reduced graphene oxide nanosheets, respectively. Going by the traditional hydrothermal technique, nanorods materials with length in several hundreds of nanometers can be synthesized as a result of gradual dissolution and recrystallization processes as well as the low growth kinetic of nanorods at static condition [15,16]. This has prompted us to develop a uniformly-stirred reflux process as demonstrated in the experimental section. The uniform stirring employed in this study speeds up the dissolution and recrystallization rates of the reduced GO nanosheets, which in turn lessens the reaction time [17].

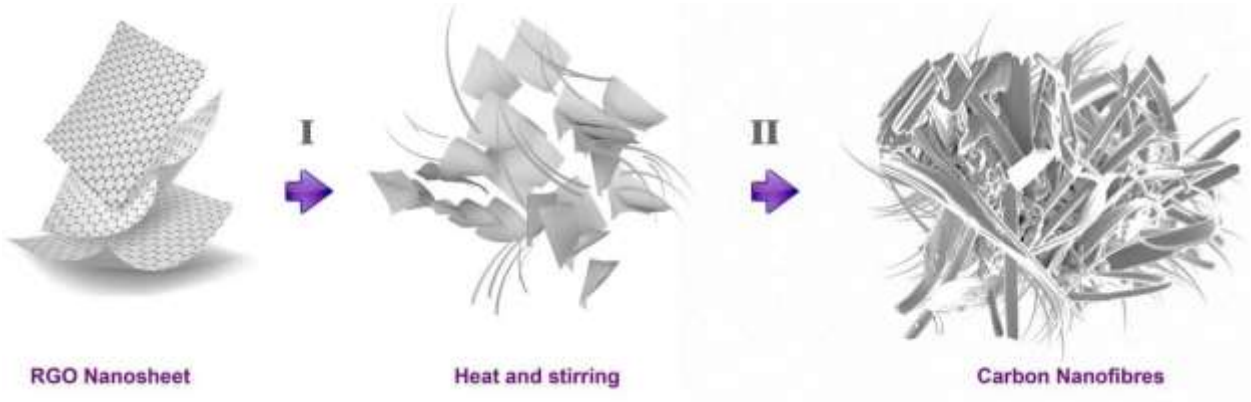

Scheme 1. Schematic of formation mechanism of the carbon nanofibres.

Scheme 1 reveals that the nanofibres are formed from the GO nanosheets, a phenomenon in line with the formation process of some similar nanotubular materials through wrapping-up of their nanosheets as reported in the literature [15–18]. Throughout the formation process, the uninterrupted growth of nanofibre is prone to a pair of shear and centripetal forces, imposed through the consistently and rapidly stirred relatively high viscous alkaline (40 wt. % NaOH) solution. During the uniform stirring, the reduced GO generated filmy materials as intermediates at the reaction temperature (130 ˚C). The shear force on the tip of the fibre-like material is assumed to be larger than on other parts over some distances off the tip besides the influence of

side force directed to the nanofibre by the axial path being insignificant as a result of the equilibrium effect, which leads to twisting of the nanofibres [17,19,20]. The shear force on the nanofibre material tip is believed to be linearly related to the stirring rate. Therefore, as soon as there is an increase in the applied force on the tip, there is a corresponding rise in the extent at which the nanofibres are bent. The required force to maintain the material mass in its circular motion, i.e. the centripetal force (F_c), increases linearly with the square of the stirring rate according to the equation [17]:

$$F_c = -4\pi^2 n^2 mr \quad (4)$$

where m is the mass, n is stirring rate, and r is radius.

A force that is equal and opposite to a resulting force away from the centre of rotation, known as the centrifugal force ($F_{cf} = 4\pi^2 n^2 mr$). This continuous force drives the sheet-like reduced GO adopted as precursor and the resulting carbon nanofibre to form in line and match continuously in the same path in the very viscous NaOH solution with no agglomeration. This quickens the nanocrystal attachment to the nanofibre end, resulting in lengthened nanofibre formation since the rate of diffusion/chemical reaction is enhanced by the high resolution stirring process. Using the SEM device, the estimated mean length of the carbon nanofibre material is observed to be ~ 40 µm. Based on the mechanism displayed in scheme 1, we noticed that the reduced GO nanosheets material precursor gave rise to the carbon nanofibre as depicted in scheme 1-I. The high rate continuous stirring accelerates a swift mass transport, which in turn enhances the degree at which the reactants diffuse. This facilitates the chemical reactions on the resulting nanofibres material as displayed in scheme 1-II, hence, lengthening the nanofibres material's structures. The shear force created via the motion of viscous NaOH solution against the nanofibre material ensured the alignment of nanofibres suspended in the solution [21], since the nanofibres re-adapt to the course of flow of the viscous solution to curtail the internal frictional

force within the solution via an inclined attachment mechanism through the share of a common crystallographic orientation [22].

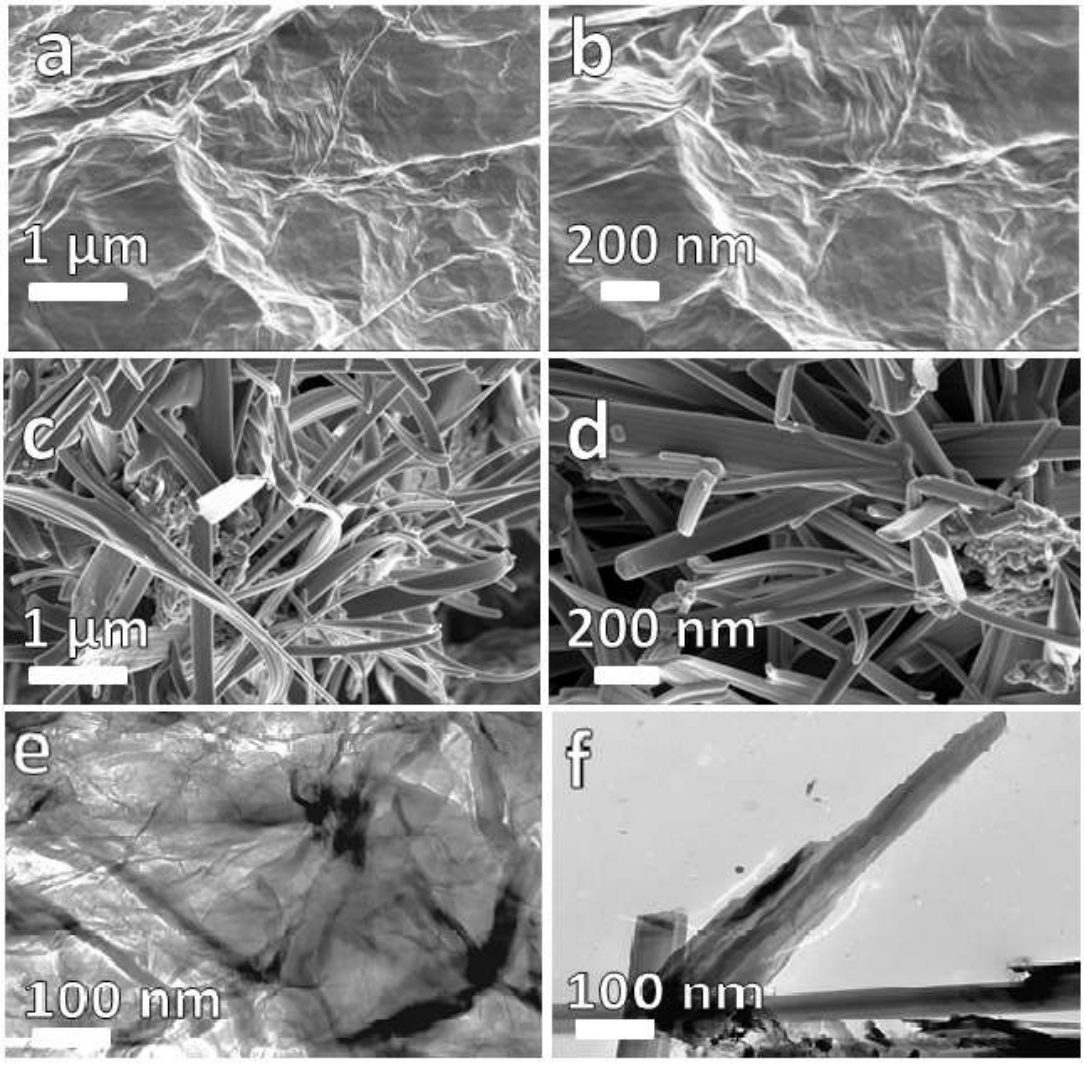

Fig. 1. SEM micrographs of (a-b) freeze-dried GO, and (c-d) GO-derived carbon nanofibres at low and high magnifications, respectively, and (e-f) TEM micrographs of freeze-dried GO and GO-derived carbon nanofibres, respectively.

Fig. 1 (a-b) shows the SEM images of the as-synthesized freeze-dried sheet-like reduced graphene oxide material at low and high magnifications before the reflux stirring process. Fig. 1 (c) and (d) display low and high magnifications SEM images of carbon nanofibres. The material

can be observed to be composed of twisted and elongated interconnected fibre-like morphology. Fig. 1 (e) and (f) display the TEM micrographs of freeze-dried sheet-like reduced graphene oxide and that of carbon nanofibres, respectively, which further confirms the successful transformation as observed from the SEM images of the materials.

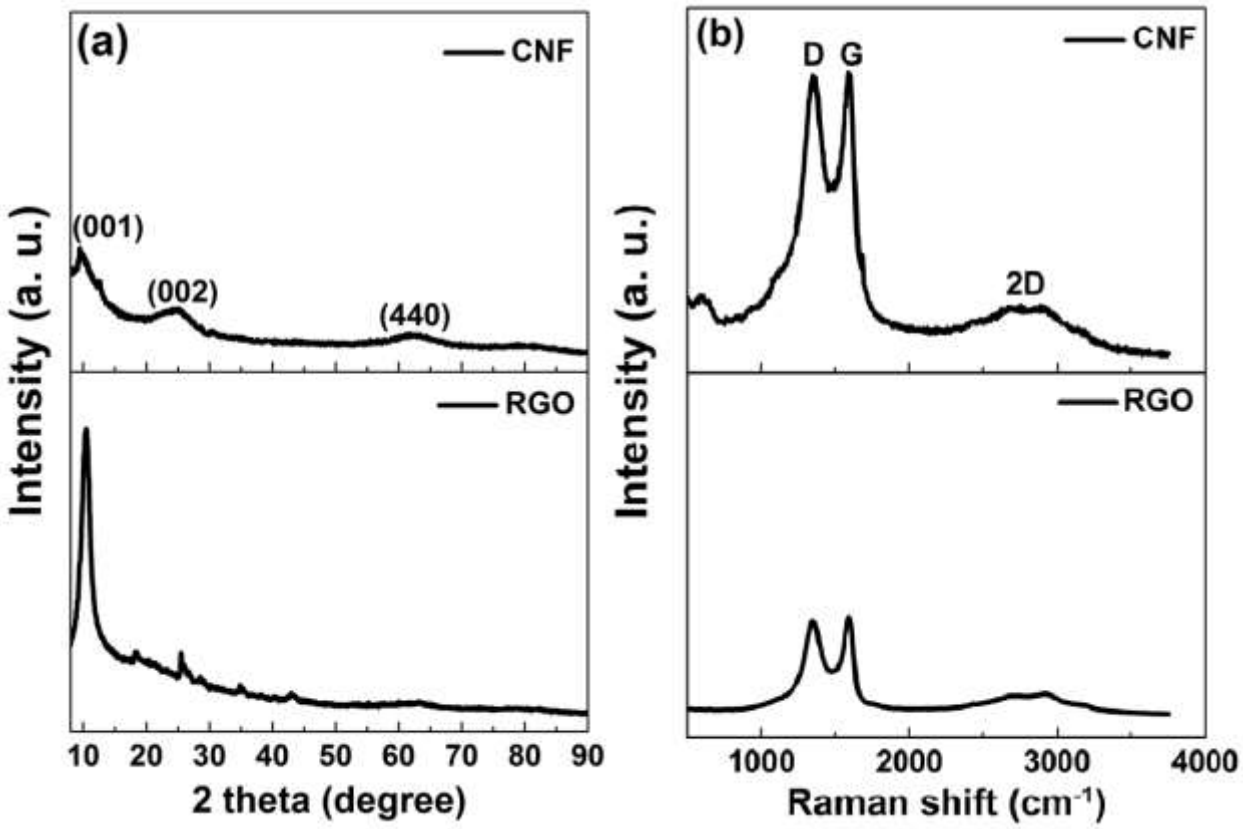

Fig. 2. (a) XRD patterns, and (b) Raman spectrum of the GO-derived carbon nanofibres (CNF) and freeze-dried RGO, respectively.

Fig. 2 (a) shows the XRD patterns of freeze-dried RGO and carbon nanofibres materials, respectively, confirming the structural compositions. The observed sharp characteristic peak at about 2θ = 10.5 ˚ corresponding to an interlayer spacing (001) of 0.84 nm is a typical of highly oxidized GO materials, indicating that the as-synthesized carbon nanofibre is free of any graphite [23]. The broad peak at around 2θ = 25.1˚, which corresponds to the (002) plane of reduced GO is evident of a disordered graphene sheets due to efficient transformation of graphite oxide to

graphene oxide [24]. The peak at nearly $2\theta = 61.7^{\circ}$; (440) plane is attributed to the silica material used as substrate in sample preparation for the analysis. The Raman spectrum in Fig. 2 (b) exhibits the characteristics distinct D and G bands peak at about 1352 and 1590 cm^{-1}, respectively, indicating a typical of graphene oxide. These D and G peaks are ascribed to defects and in-plane vibration of sp^2 carbon atoms in the material's structure, respectively. The D-G peak (I_D/I_G) intensity ratio of the material was calculated to be 0.99, establishing a moderate degree of graphitization and/or density of defects in the nanofibre material. The 2D band peak observed at nearly 2699 cm^{-1} is attributed to the multisheet-like reduced GO adopted for carbon nanofibre material synthesis, and further confirms the nanofibre crystalline nature [25].

Fig. 3 shows analysis from XPS measurements adopted for deducing the material's chemical composition. Fig. 3(a) shows the wide scan XPS spectra of the carbon nanofibre. The figure displays the principal elements namely C (285.13 eV), and O (534.1 eV) that make up the nanomaterial. The C to O ratio was determined via the survey spectra, and is estimated to be ~ 1.87. A trace of Na shown by the material can be attributed to high concentration NaOH solution employed as base fluid in sample preparation. The noticeable Auger oxygen (O) peak at ~ 978.7 eV is a representative of energy of the electrons discharged from atoms of the material owing to the O 1s state filling; an electron from the L-shell filling the K-shell, combined with an electron being discharged from an L-shell. Such peak results from the degeneration of a more active

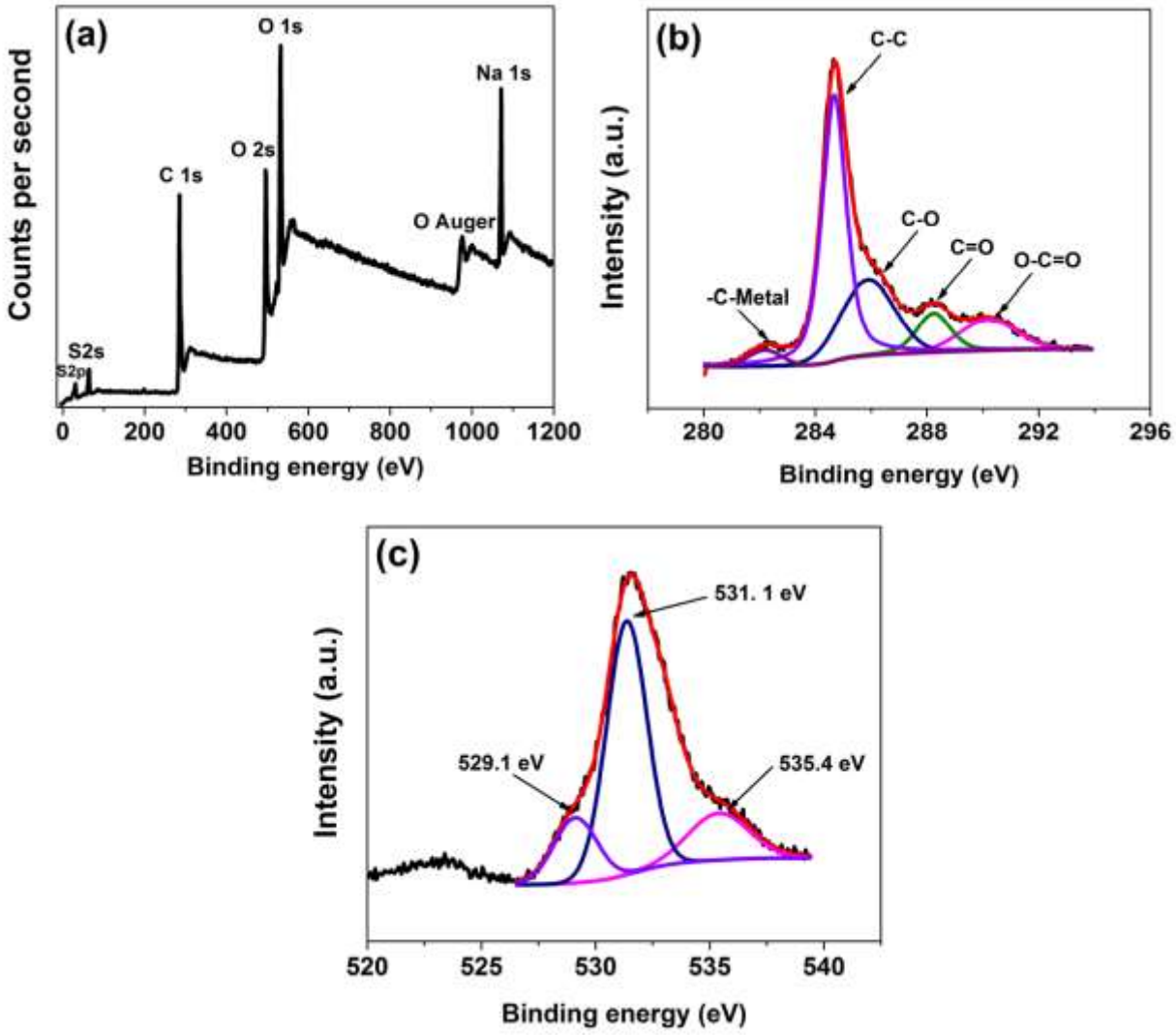

Fig. 3. (a) XPS survey spectra, core level spectrum of (b) C 1s, and (c) O 1s of as-synthesized carbon nanofibre material.

electron filling the available hole resulting from the x-ray photon alongside an emission by a characteristic energy of the difference between the states comprised in the process [26,27]. Table S1 *(see supporting information)* shows the XPS elemental analysis of the carbon nanofibres with atomic concentrations of 73.58 at% C 1s, and 26.42 at% O 1s. From 3(b), an estimated full width at half maximum (FWHM) of ~ 0.76 eV is observed as principal sp^2 carbon peak for the material. A value that is comparable to those of fits in highly oriented graphitic carbon.

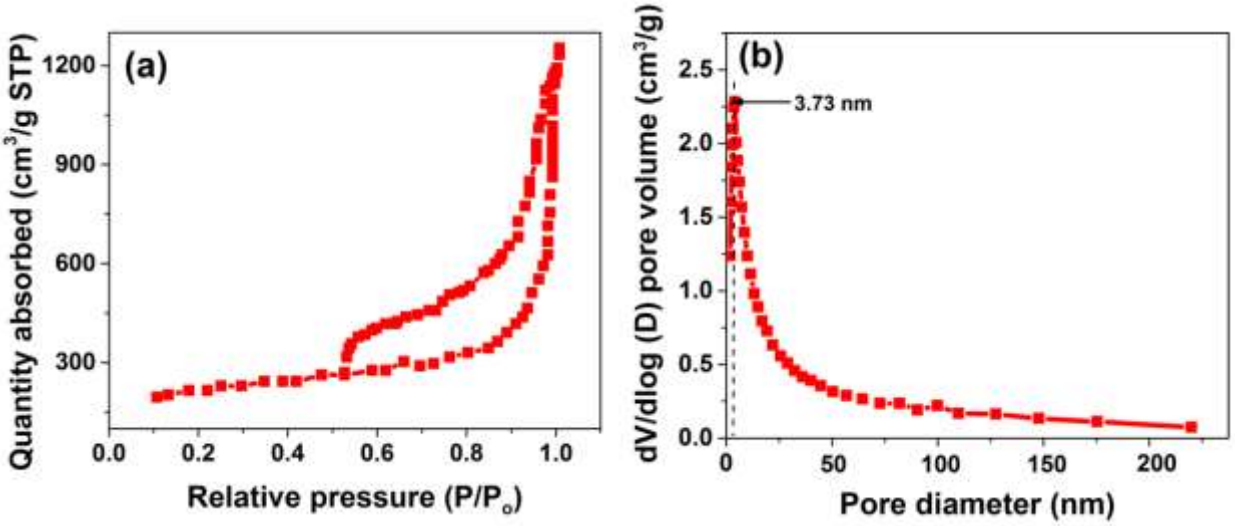

Fig. 4. (a) N_2 isotherms, and (b) pore size distribution of GO-derived carbon nanofibres.

In Fig. 3(b), four major peaks namely, carbon bond; C–C (284.7 eV), epoxy group; C–O (286.1 eV), carbonyl group; C=O (288.3 eV), carboxyl group; O-C=O (290.2 eV), and carbon-metal group; -C-Na (282.1 eV) are noticed at various functional groups of carbon atoms. Also, Fig. 3(c) is a display of the core level spectrum of O 1s with fitted peaks visible at about 529.1, 531.4 and 535.3 eV, which can be assigned to O 1s in C–O composition. The reported binding energies for this material are in line with other carbon-based materials reported in the literature [25,28–31].

Fig. 4(a) depicts the type-IV N_2 isotherms of carbon nanofibre derived at standard temperature and pressure, STP. This figure indicates a specific surface area of about 1317.8 m^2 g^{-1} for the material. The observed H3 hysteresis between adsorption and desorption isotherms alongside a sharp drop, at higher relative pressures in the adsorbed amount is ascribed to the mesoporous nature of the sheet-like reduced GO-derived carbon nanofibres [29]. Figure 4(b) displays desorption pore-size distribution of the material determined via BJH technique, indicating clearly the average pore size distribution showing a peak at nearly 3.73 nm. This higher average pore

size of the carbon nanofibre compared to the dimension of ions of the ionic liquid electrolyte, which is approximately 0.7 nm, allows for ions accommodation within the pores of the material. Therefore, resulting in improved electrolyte accessibility and enhanced charge storage process.

Electrochemical measurements

Standard two-electrode measurements of symmetric cells

The ideal electrochemical properties along with the working condition for the as-synthesized carbon nanofibre electrode material were first investigated in a three-electrode configuration to ascertain the materials optimum operational potential range among other properties, results of which are shown as Fig. S1 in the supporting information. Fig. S1 (a) (see supporting information) depicts the CV curves measured in a three-electrode configuration to study the ideal working condition and electrochemical behaviour of the as-synthesized carbon nanofibres electrode material in both the negative and positive operating potentials. It could be observed that the material could satisfactorily operate in a reversible potential window. A wider operating potential of ~ 1.5V was observed for the material in ILE compared to ~ 0.4V in both the 1 M Na_2SO_4 and 6 M KOH electrolytes, respectively. Fig. S1 (b) shows the CV curves of freeze-dried RGO electrode measured as a half-cell. The material displayed lower current responses in all three electrolytes compared the carbon nanofibres, showing the superiority of the carbon nanofiber material over the freeze-dried RGO. Using equation ES1 in the supporting information, the freeze-dried RGO sample could yield a specific capacitance values of 71.8, 63.5 and 54.2 F g^{-1}, respectively, compared to 88.1, 69.3 and 62.5 F g^{-1} observed for the carbon nanofibres in 6 M KOH, 1 M Na_2SO_4 and ILE electrolytes at a scan rate of 50 mVs^{-1}, respectively, based on the mass of active material. The observed values showed the carbon nanofibre enhanced performance over the freeze-dried RGO material.

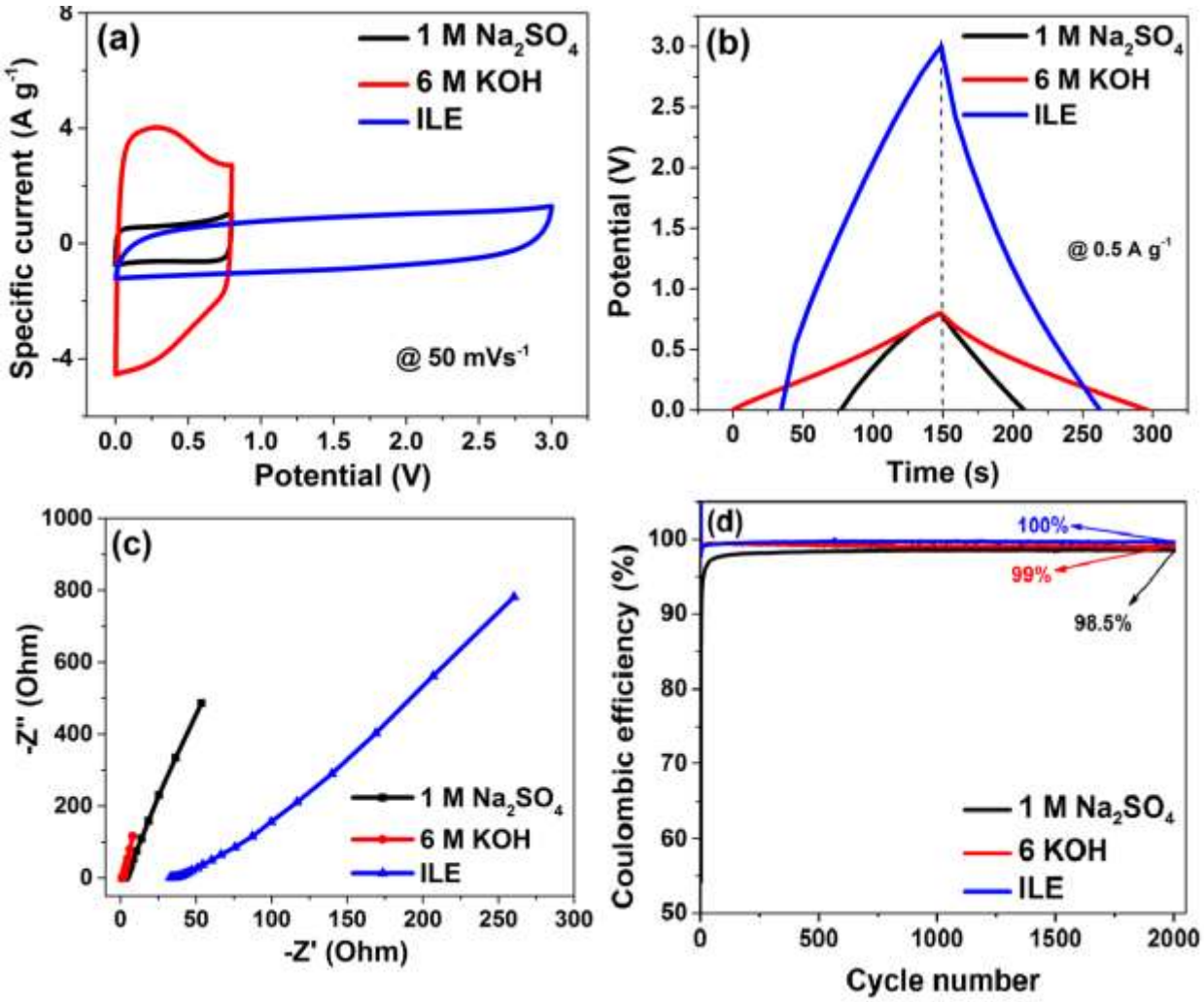

Fig. 5. (a) CV profiles, (b) GCD profiles, (c) Nyquist spectra, and (d) coulombic efficiency for carbon nanofibers symmetric cells operating in 1 M Na_2SO_4, 6 M KOH and ILE, respectively.

Fig. 5 (a) compares the CV curves of the carbon nanofibres in the three different electrolytes already stated in the earlier section of the paper at a scan rate of 50 mV s^{-1}. A higher current response was observed for the 6 M KOH compared to the other two electrolytes. This can be attributed to the higher ions motilities and active proton transport process of K metal compared to that of Na in 1 M Na_2SO_4, which shows less efficient charge propagation [32,33]. From the figure, a protic1-ethylimidazolium bis(trifluoromethanesulfonyl)imide ionic liquid electrolyte designated as ILE could operate well over a much wider operational potential of ~ 3V compared

to 0.8V for both 6 M KOH and 1 M Na_2SO_4 aqueous electrolytes. The much wider electrochemical potential of up to ~ 3V is ascribed to electrochemical stability of the ions in the ILE due to its higher viscosity masking the decomposition compared to the OH-ions and water molecules. The selected ILE for these measurements also has other beneficial properties such as high ionic density, non-volatility, moderate ionic conductivity, non-flammability and non-corrosiveness among others [34]. The ions making up the ionic liquid electrolyte in this study are more stable than water based electrolytes, which gives it a wider operating potential. The pure ionic liquid electrolyte has no sensitive solvents that would decompose or evaporate. Besides, the ionic interactions between the ions are much stronger than in solvents and thus, prevent the molecules from evaporating. The behavior observed for the material in Fig. 5 (a) for all the electrolytes is also confirmed by the results of the GCD curves displayed in Fig. 5 (b) measured at a specific current of 0.5 A g^{-1}. Fig. 5 (c) depicts the EIS Nyquist spectra for the carbon nanofibres symmetric cells operating in 6 M KOH, 1 M Na_2SO_4 and ILE electrolytes, performed at a potential of 0.0 V and the frequency range of 10 mHz –100 kHz. The plots in Fig. 5 (c) shows similar trends as observed by other techniques in Fig. 5 (a and b). The Nyquist plot in Fig. 5 (c) is a representative of a typical capacitive material showing diffusion differences in the electrochemical properties of the symmetric cells operating in the three different electrolytes. The best results were observed for a cell operating in 6 M KOH electrolyte with real part impedance (-Z') also known as the equivalent series resistance, Rs value of 0.43 Ω in the high frequency region, compared to 0.66 Ω and 26.41 Ω for 1 M Na_2SO_4 and ILE electrolytes, respectively. The low impedance value of 0.43 Ω observed for the cell in 6 M KOH is attributed to the higher mobility and diffusion coefficient of the K^+ compared to the Na^+. In this case of ILE, the flow of ion is slower, which could be ascribed to the electrolyte's high viscosities that limit the charge transportation speed as well as the accessibility of the electrolyte to smaller pores in the electrode surface [35], since the ions in the ILE are much larger in size than the Na-

and K-ions. Fig. 5 (d) compares the device coulombic efficiencies measured at a specific current of 5.0 A g^{-1} over 2000 cycling in the three selected electrolytes, showing an efficiency of ~ 100%, 99% and 98.5% for the cell operated in in ILE, 6 M KOH and 1 M Na_2SO_4, respectively, showing the ILE high stability over the 6 M KOH and 1 M Na_2SO_4 electrolytes. The symmetric device operated in ILE is of advance interest for supercapacitor application due to its wider operating potential, non-corrosiveness and long cycle stability (see Fig. 7 (d)).

Fig. 6(a and b) presents the specified electrochemical behaviour of the carbon nanofibres symmetric cells with a characteristic CV and GCD profiles investigated at different scan rates and specific currents range from 5 to 100 mV s^{-1} and 0.5 to 10 A g^{-1} in a 1-ethylimidazolium bis(trifluoromethanesulfonyl)imide ionic liquid electrolyte (ILE). The CV and GCD profiles are both notably rectangular and symmetrical, respectively, a feature confirming the capacitive nature of the material's symmetric cells. The results obtained for the device in this work compares well to the supercapacitor performances reported from other groups on similar materials from the literature [36–42]. The electrical resistance of the symmetric carbon nanofibres device was further estimated via the electrochemical impedance spectroscopy (EIS) at a potential of 0.0 V and a frequency range of 10 mHz –100 kHz. Fig. 6 (c) shows the Nyquist impedance plot of the device fitted by adopting a ZFIT fitting program v11.02 with its equivalent circuit depicted in Fig. 6 (d). The Nyquist plot can be noticed to display a noticeable semicircle in the high frequency region which can be ascribed to interfacial charge transfer resistance and mass transport via the device's electrode material [37,43]. From Fig. 6 (d), R_1 denotes the device's equivalent series resistance and is found to be ~ 10 Ω, R_2 characterizes the charge transfer resistance between the interface of the test solution and carbon nanofibres material, the constant phase elements Q_1 and Q_3 employed in place of capacitors describe the double layer capacitance at the interface, and the pseudo capacitance from ions transfer in the carbon nanofibres matrix [37,38,43–45]. The low equivalent series resistance indicates good

conductivity that is really favorable for fast redox systems in the device [37,44-47]. Q_3 is connected in parallel with a single resistance, R_3. Fig. S2 in the supporting information portrays the full CV and GCD profiles of the carbon nanofibers symmetric cells in both 6 M KOH and 1 M Na_2SO_4 aqueous electrolytes, respectively, with both showing the characteristics electrochemical double-layer capacitive (EDLC) nature. All the CV-GCD profiles match well with the results shown in Fig. 5.

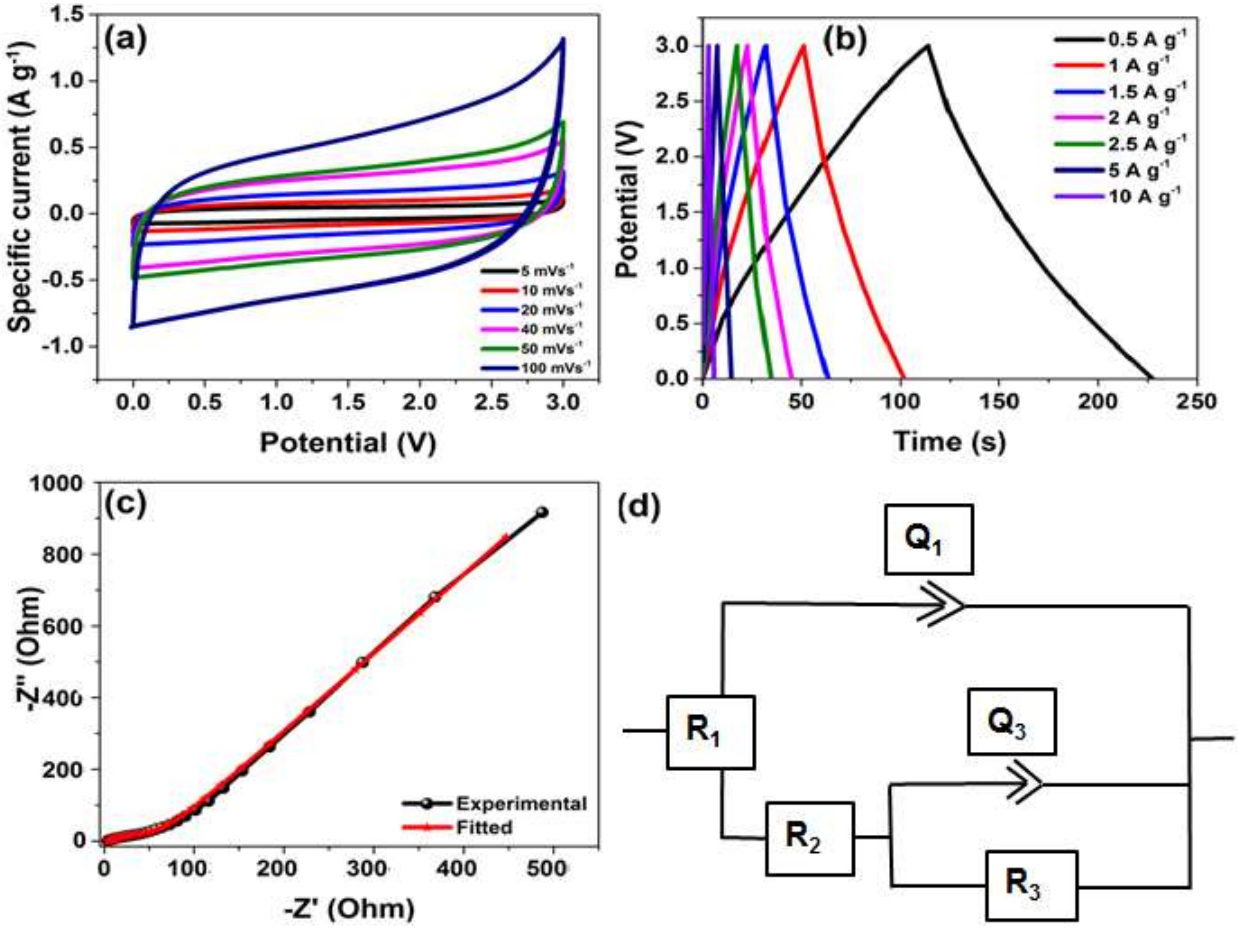

Fig. 6. (a) CV profiles at different scan rates, (b) GCD profiles at different specific currents densities in ILE, (c) fitted Nyquist plot and (d) the equivalent circuit for the carbon nanofibres device, respectively.

Fig. 7 (a) compares the specific capacitances of the cell computed through equation 1 and plotted as a function of specific currents. The full cell exhibits a maximum specific capacitance of 362.8,

147.5, and 77.1 F g^{-1} at a specific current of 0.5 A g^{-1} in 6 M KOH, 1 M Na_2SO_4 and ILE solutions, respectively. Interestingly, the symmetric cells can preserve a high specific capacitances of 310, 120, and 53.3 F g^{-1}, respectively, even when the specific current is multiplied by a factor of 20 (10 A g^{-1}), implying that ~85.5%, 81.4% and 69.1% of its initial capacitance can be retained, respectively, when the specific current is increased by 20 folds. The enhanced performance of the cell in 6 M KOH and 1 M Na_2SO_4 over the ILE can be attributed to the alkali metal ions being strongly solvated in solution. Besides, the high mobility and diffusion coefficients characterized by the K^+ and Na^+ provide for fast ion diffusion rate within the electrode/electrolyte interface [32]. The Ragone plot in Fig. 7 (b) is a representation of the cell's position in the various electrolytes in terms of both energy and power densities, which are perceived to be two decisive parameters that determine the practicability of a supercapacitor. Using equations 2 and 3, the energy densities of the devices based on masses of the active materials were calculated to be ~ 24.0 Wh kg^{-1}, 8.1 Wh kg^{-1}, and 3.3 Wh kg^{-1} with corresponding power densities of 750.3 W kg^{-1}, 197.4 W kg^{-1}, and 200 W kg^{-1} for ILE, 6 M KOH, and 1 M Na_2SO_4 electrolytes, respectively, at of 0.5 A g^{-1}. The higher value of energy and power densities observed for the ILE compared to 6 M KOH and 1 M Na_2SO_4 solutions can be ascribed to the electrolyte's higher operating potential due to its higher electrochemical stability as compared to aqueous based electrolytes. This wider electrochemical window alongside moderate electrical conductivity results in high energy and power densities recorded for the material. Fig. 7 (c) is a Ragone chart depicting the position of the symmetric device in this work compared to some other similar materials recently published in the literature, based on their energy and power densities. Such materials include, RGO-based supercapacitor device; 11.6 Wh kg^{-1} at power density of 13900 W kg^{-1}, at 0.5 A g^{-1}[36], 3D hierarchical RGO nanosheets; 12.4 Wh kg^{-1} at power density of 1600 W kg^{-1}, at 1 A g^{-1}[48], Modified RGO hydrogels; 8.02 Wh kg^{-1} at power density of 125 W kg^{-1}, at 0.05 A g^{-1}[49], N-doped porous carbon nanofibers; 7.11 Wh kg^{-1} at

power density of 10200 W g^{-1}, at 0.25 A g^{-1}[50]; Porous carbon nanofibers; 4.0 Wh kg^{-1} at power density of 20000 W kg^{-1}, at 1 A g^{-1}[51] and Electrochemically tailored 3D RGO networks; 11.2 Wh kg^{-1} at power density of 5000 W kg^{-1}, at 1 A g^{-1}[52].

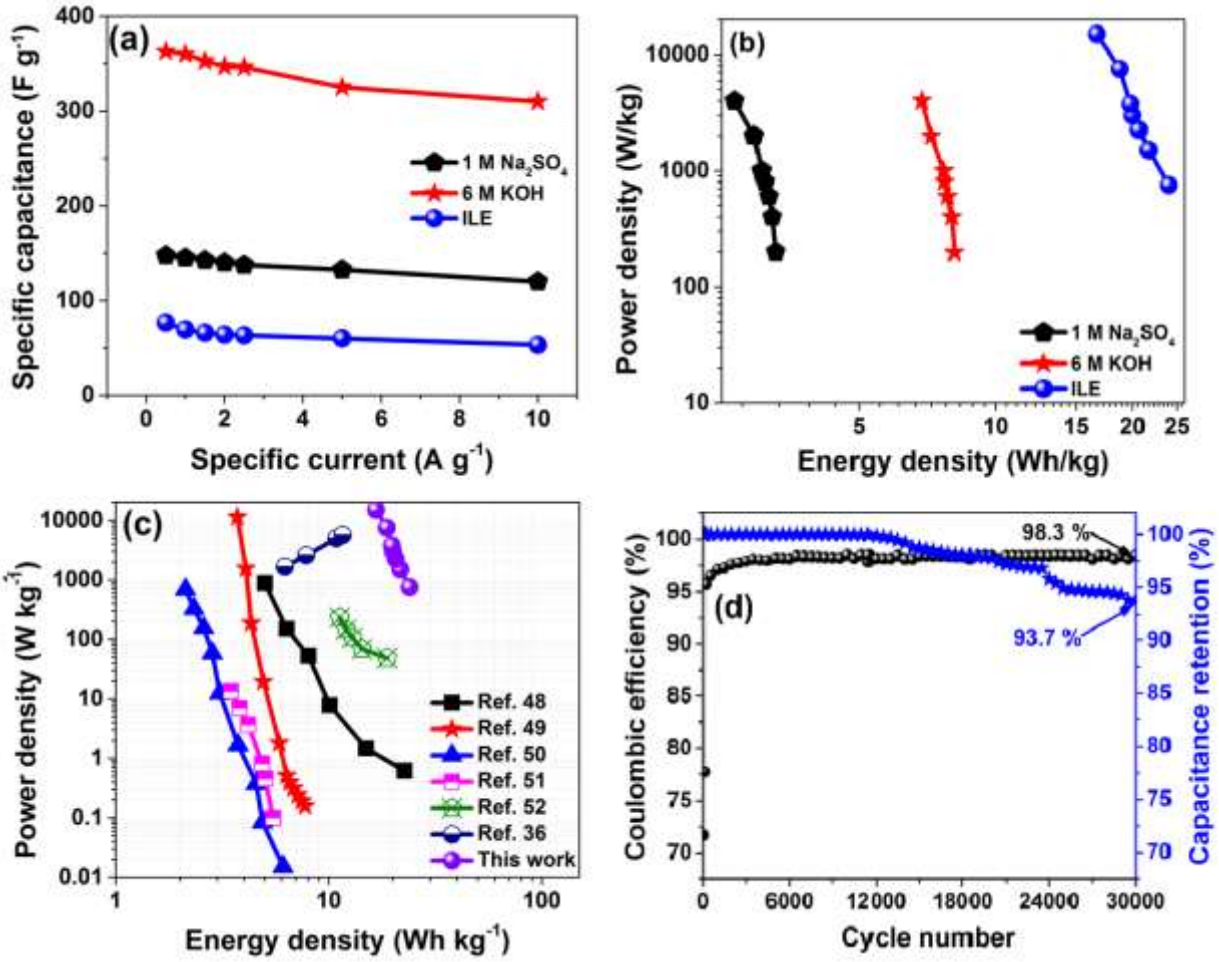

Fig. 7. (a) Plots of specific capacitance at various specific currents, and (b) Ragone plots in different electrolytes, (c) Ragone comparison to other similar carbon material electrodes from the literature, and (d) cyclic performances against cycle numbers for carbon nanofibers symmetric cell.

The figure shows that the results obtained for this device are comparatively appropriate to some other related carbon-based supercapacitors cited from literature. More-over, the GCD technique was adopted to study the long-term operation and stability of the carbon nanofibres symmetric device at a specific current of 5.0 A g^{-1} using the ILE electrolyte for over an extended cycling

test of 30,000 cycles. The result of which is shown in Fig. 7 (d). A capacitance fading noticed at beyond 12000 cycles of cycling test is attributed to the very high potential (3.0 V) applied to the device as well as the electrochemical degradation of the electrode material due to the large number of cycling. Nonetheless, the device was observed to proof a significant coulombic efficiency of around 98.3%, with about 93.7% of its initial capacitance being retained after cycling for over 30,000 cycles. This excellent cycling stability is attributed to the ILE high ionic density, non-volatility and low vapor pressure alongside the material's porous structure.

Conclusion

Novel carbon nanofibres produced from freeze-dried sheet-like RGO was successfully developed through an innovative, simple and scalable stirring reflux process. Results obtained from the analysis show that the force-driven reflux technique adopted has efficiently subdue the agglomeration of RGO nanosheets thereby, creating fibre-like porous material structures with enhanced ion diffusion process. Besides, an assembled symmetric SC from the carbon nanofibre and ILE electrolyte, portrayed a wider operating potential of about 3.0 V, high energy and power densities (24.0 Wh kg^{-1} and 750.3 W kg^{-1}) compared to 0.8 V, energy and power densities (3.3 Wh kg^{-1} and 200 W kg^{-1}), and (8.1 Wh kg^{-1} and 197.4 W kg^{-1}) for 1 M Na_2SO_4 and 6 M KOH electrolytes, respectively, at a specific current of 0.5 A g^{-1}. The unique stability of the material in ILE displayed its possibility and efficacy as electrode materials for energy storage and conversion devices applications.

Acknowledgements

South African Research Chairs Initiative of the Department of Science and Technology (DST) and National Research Foundation (NRF) of South Africa (Grant No. 61056). Every finding and conclusion expressed in this work is of the author(s), and the NRF does not accept any liability in this regard. The grant No. SA2016-6762 "High Energy Density and Power: Hybrid

Supercapacitors from Renewable Sources" from the Swedish Foundation for International Cooperation in Research and Higher Education within the South Africa-Sweden Bilateral Scientific Research Cooperation Programme is gratefully acknowledged. K. O. is grateful to Dr. Farshad Barzegar of the University of Pretoria for his inputs.

References

[1] B. Kang, G. Ceder, Battery materials for ultrafast charging and discharging, Nature. 458 (2009) 190–193. doi:10.1038/nature07853.

[2] H. Zhang, X. Yu, P. V Braun, Three-dimensional bicontinuous ultrafast-charge and -discharge bulk battery electrodes, Nat. Nanotechnol. (2011) 1–5. doi:10.1038/NNANO.2011.38.

[3] Z. Fan, J. Yan, T. Wei, L. Zhi, G. Ning, T. Li, F. Wei, Asymmetric supercapacitors based on graphene/MnO2 and activated carbon nanofiber electrodes with high power and energy density, Adv. Funct. Mater. 21 (2011) 2366–2375. doi:10.1002/adfm.201100058.

[4] H. Chen, L. Hu, Y. Yan, R. Che, M. Chen, L. Wu, One-step fabrication of ultrathin porous nickel hydroxide-manganese dioxide hybrid nanosheets for supercapacitor electrodes with excellent capacitive performance, Adv. Energy Mater. 3 (2013) 1636–1646. doi:10.1002/aenm.201300580.

[5] S. Liu, H. Jia, L. Han, J. Wang, P. Gao, D. Xu, J. Yang, S. Che, Nanosheet-constructed porous TiO2-B for advanced lithium ion batteries, Adv. Mater. 24 (2012) 3201–3204. doi:10.1002/adma.201201036.

[6] J. K. Wassei, R.B. Kaner, Graphene, a promising transparent conductor, Mater. Today. 13 (2010) 52–59. doi:10.1016/S1369-7021(10)70034-1.

[7] W. Lv, Z. Li, Y. Deng, Q.-H. Yang, F. Kang, Graphene-based materials for electrochemical energy storage devices: Opportunities and challenges, Energy Storage Mater. 2 (2016) 107–138. doi:10.1016/j.ensm.2015.10.002.

[8] A. Abouimrane, O.C. Compton, K. Amine, S.T. Nguyen, Non-annealed graphene paper as a binder-free anode for lithium-ion batteries, J. Phys. Chem. C. 114 (2010) 12800–12804. doi:10.1021/jp103704y.

[9] N. Zhu, W. Liu, M. Xue, Z. Xie, D. Zhao, M. Zhang, J. Chen, T. Cao, Graphene as a conductive additive to enhance the high-rate capabilities of electrospun $Li_4Ti_5O_{12}$ for lithium-ion batteries, Electrochim. Acta. 55 (2010) 5813–5818. doi:10.1016/j.electacta.2010.05.029.

[10] G. Wang, B. Wang, X. Wang, J. Park, S. Dou, H. Ahn, K. Kim, Sn/graphene nanocomposite with 3D architecture for enhanced reversible lithium storage in lithium ion batteries, J. Mater. Chem. 19 (2009) 8378–8384. doi:10.1039/b914650d.

[11] A. Zurutuza, C. Marinelli, "Challenges and opportunities in graphene commercialization",

Nature nanotechnology 9 (2014) 730-734. doi: 10.1038/nnano.2014.225.

[12] K. O. Oyedotun, M.J. Madito, A. Bello, D.Y. Momodu, A.A. Mirghni, N. Manyala, Investigation of graphene oxide nanogel and carbon nanorods as electrode for electrochemical supercapacitor, Electrochim. Acta. 245 (2017) 268–278. doi:10.1016/j.electacta.2017.05.150.

[13] K. O. Oyedotun, F. Barzegar, A. A. Mirghni, A. A. Khaleed, T. M. Masikhwa, N. Manyala, Examination of High-Porosity Activated Carbon Obtained from Dehydration of White Sugar for Electrochemical Capacitor Applications, ACS Sustain. Chem. Eng. 7 (2019) 537–546. doi:10.1021/acssuschemeng.8b04080.

[14] F. Barzegar, A. A. Khaleed, F. U. Ugbo, K. O. Oyeniran, D. Y. Momodu, A. Bello, J. K. Dangbegnon, N. Manyala, Cycling and floating performance of symmetric supercapacitor derived from coconut shell biomass, AIP Adv. 6 (2016) 115306. doi:10.1063/1.4967348.

[15] L. Torrente-Murciano, A. A. Lapkin, D. Chadwick, Synthesis of high aspect ratio titanate nanotubes, J. Mater. Chem. 20 (2010) 6484-6489. doi:10.1039/c0jm01212b.

[16] T. Kijima, Inorganic and Metallic Nanotubular Materials: Recent Technologies and Applications, Top. Appl. Phys. 117 (2010) 17–32. doi:10.1007/978-3-642-03622-4.

[17] Y. Tang, Y. Zhang, J. Deng, J. Wei, H. Le Tam, B.K. Chandran, Z. Dong, Z. Chen, X. Chen, Mechanical force-driven growth of elongated bending Tio2-based nanotubular materials for ultrafast rechargeable lithium ion batteries, Adv. Mater. 26 (2014) 6111–6118. doi:10.1002/adma.201402000.

[18] T. Kasuga, M. Hiramatsu, A. Hoson, T. Sekino, K. Niihara, Formation of Titanium Oxide Nanotube, Langmuir. 14 (1998) 3160–3163. doi:10.1021/la9713816.

[19] B. Xie, H. Zhang, H. Kan, S. Liu, M.Y. Li, Z. Li, S. Zhu, S. Qiu, S. Jiang, Mechanical force-driven growth of elongated BaTiO3lead-free ferroelectric nanowires, Ceram. Int. 43 (2017) 2969–2973. doi:10.1016/j.ceramint.2016.11.049.

[20] D. V. Bavykin, J.M. Friedrich, F.C. Walsh, Protonated titanates and TiO2nanostructured materials: Synthesis, properties, and applications, Adv. Mater. 18 (2006) 2807–2824. doi:10.1002/adma.200502696.

[21] Y. Z. Long, M. Yu, B. Sun, C. Z. Gu, Z. Fan, Recent advances in large-scale assembly of semiconducting inorganic nanowires and nanofibers for electronics, sensors and photovoltaics, Chem. Soc. Rev. 41 (2012) 4560–4580. doi:10.1039/c2cs15335a.

[22] J. M. McHale, A. Auroux, A. J. Perrotta, A. Navrotsky, Surface energies and thermodynamic phase stability in nanocrystalline aluminas, Science. 277 (1997) 788–789. doi:10.1126/science.277.5327.788.

[23] Y. Xu, H. Bai, G. Lu, C. Li, G. Shi, Flexible graphene films via the filtration of water-soluble noncovalent functionalized graphene sheets, J. Am. Chem. Soc. 130 (2008) 5856–5857. doi:10.1021/ja800745y.

[24] M. M. Shahid, A. Pandikumar, A. M. Golsheikh, N. M. Huang, H. N. Lim, Enhanced electrocatalytic performance of cobalt oxide nanocubes incorporating reduced graphene oxide as a modified platinum electrode for methanol oxidation, RSC Adv. 4 (2014)

62793–62801. doi:10.1039/c4ra08952a.

[25] W. K. Park, Y. Yoon, Y. H. Song, S. Y. Choi, S. Kim, Y. Do, J. Lee, H. Park, D. H. Yoon, W.S. Yang, High-efficiency exfoliation of large-area mono-layer graphene oxide with controlled dimension, Sci. Rep. 7 (2017) 16414. doi:10.1038/s41598-017-16649-y.

[26] T. Xps, XPS Spectra, *. (2013) 1–77. www.casaxps.com (accessed December 19, 2018).

[27] M. A. P. Arce, Growth of High Permittivity Dielectrics by High Pressure Sputtering from metalic targets, Springer. 2017. doi:10.1007/978-3-319-66607-5.

[28] C. M. Chen, Q. Zhang, M. G. Yang, C. H. Huang, Y. G. Yang, M. Z. Wang, Structural evolution during annealing of thermally reduced graphene nanosheets for application in supercapacitors, Carbon N. Y. 50 (2012) 3572–3584. doi:10.1016/j.carbon.2012.03.029.

[29] S. Kannappan, K. Kaliyappan, R. K. Manian, A. S. Pandian, H. Yang, Y. S. Lee, J. -H. Jang, W. Lu, Graphene based Supercapacitors with Improved Specific Capacitance and Fast Charging Time at High Current Density, arXiv preprint arXiv:1311.1548 (2013).

[30] R. Yuksel, B. Yarar Kaplan, E. Bicer, A. Yurum, S. Alkan Gursel, H.E. Unalan, All-carbon hybrids for high performance supercapacitors, Int. J. Energy Res. 42 (2018) 3575–3587. doi:10.1002/er.4103.

[31] K. Muthoosamy, R. Geetha Bai, I. B. Abubakar, S. M. Sudheer, H. N. Lim, H. S. Loh, N. M. Huang, C.H. Chia, S. Manickam, Exceedingly biocompatible and thin-layered reduced graphene oxide nanosheets using an eco-friendly mushroom extract strategy, Int. J. Nanomedicine. 10 (2015) 1505–1519. doi:10.2147/IJN.S75213.

[32] K. Fic, G. Lota, M. Meller, E. Frackowiak, Novel insight into neutral medium as electrolyte for high-voltage supercapacitors, Energy Environ. Sci. 5 (2012) 5842–5850. doi:10.1039/C1EE02262H.

[33] Q. Pan, W. Tu, L. Ding, G. Mi, Characteristics of electric double layer in different aqueous electrolyte solutions for supercapacitors, Wuhan Univ. J. Nat. Sci. 17 (2012) 200–204. doi:10.1007/s11859-012-0828-1.

[34] T. Sato, G. Masuda, K. Takagi, Electrochemical properties of novel ionic liquids for electric double layer capacitor applications, Electrochim. Acta. 49 (2004) 3603–3611. doi:10.1016/j.electacta.2004.03.030.

[35] M. Galiński, A. Lewandowski, I. Stepniak, Ionic liquids as electrolytes, Electrochim. Acta. 51 (2006) 5567–5580. doi:10.1016/j.electacta.2006.03.016.

[36] M. Down, S. J. Rowley-Neale, graham Smith, C.E. Banks, Fabrication of Graphene Oxide Supercapacitor Devices, ACS Appl. Energy Mater. 1 (2018) 707-714. doi:10.1021/acsaem.7b00164.

[37] F. B. Ajdari, E. Kowsari, A. Ehsani, M. Schorowski, T. Ameri, New synthesized ionic liquid functionalized graphene oxide: Synthesis, characterization and its nanocomposite with conjugated polymer as effective electrode materials in an energy storage device, Electrochim. Acta. 292 (2018) 789–804. doi:10.1016/j.electacta.2018.09.177.

[38] A. Ehsani, E. Kowsari, M. Dashti Najafi, R. Safari, H. Mohammad Shiri, Influence of

ionic liquid on pseudocapacitance performance of electrochemically synthesized conductive polymer: Electrochemical and theoretical investigation, J. Colloid Interface Sci. 500 (2017) 315–320. doi:10.1016/j.jcis.2017.04.014.

[39] X. He, N. Zhang, X. Shao, M. Wu, M. Yu, J. Qiu, A layered-template-nanospace-confinement strategy for production of corrugated graphene nanosheets from petroleum pitch for supercapacitors, Chem. Eng. J. 297 (2016) 121–127. doi:10.1016/j.cej.2016.03.153.

[40] S. Dong, X. He, H. Zhang, X. Xie, M. Yu, C. Yu, N. Xiao, J. Qiu, Surface modification of biomass-derived hard carbon by grafting porous carbon nanosheets for high-performance supercapacitors, J. Mater. Chem. A. 6 (2018) 15954–15960. doi:10.1039/c8ta04080j.

[41] X. He, X. Li, H. Ma, J. Han, H. Zhang, C. Yu, N. Xiao, J. Qiu, ZnO template strategy for the synthesis of 3D interconnected graphene nanocapsules from coal tar pitch as supercapacitor electrode materials, J. Power Sources. 340 (2017) 183–191. doi:10.1016/j.jpowsour.2016.11.073.

[42] X. He, H. Zhang, K. Xie, Y. Xia, Z. Zhao, X. Wang, Synthesis of mesoporous carbons from rice husk for supercapacitors with high energy density in ionic liquid electrolytes. Journal of nanoscience and nanotechnology, 16 (3), 2841-2846. doi.org/10.1166/jnn.2016.12467.

[43] W. Sun, X. Chen, Preparation and characterization of polypyrrole films for three-dimensional micro supercapacitor, J. Power Sources. 193 (2009) 924–929. doi:10.1016/j.jpowsour.2009.04.063.

[44] J. Torabian, M.G. Mahjani, H. Mohammad Shiri, A. Ehsani, J. Shabani Shayeh, Facile electrosynthesis, characterisation and electrochemical performance of poly: Ortho aminophenol/Al5Y3O12 nanocomposite as a new high efficient supercapacitor, RSC Adv. 6 (2016) 41045–41052. doi:10.1039/c6ra03330j.

[45] L. Shen, L. Du, S. Tan, Z. Zang, C. Zhao, W. Mai, Flexible electrochromic supercapacitor hybrid electrodes based on tungsten oxide films and silver nanowires, Chem. Commun. 52 (2016) 6296–6299. doi:10.1039/c6cc01139j.

[46] H. Mohammad Shiri, A. Ehsani, Electrosynthesis of neodymium oxide nanorods and its nanocomposite with conjugated conductive polymer as a hybrid electrode material for highly capacitive pseudocapacitors, J. Colloid Interface Sci. 495 (2017) 102–110. doi:10.1016/j.jcis.2017.01.097.

[47] H. S. Chavan, B. Hou, A. T. A. Ahmed, Y. Jo, S. Cho, J. Kim, S. M. Pawar, S. N. Cha, A. I. Inamdar, H. Im, H. Kim, Nanoflake $NiMoO_4$ based smart supercapacitor for intelligent power balance monitoring, Sol. Energy Mater. Sol. Cells. 185 (2018) 166–173. doi:10.1016/j.solmat.2018.05.030.

[48] M. Wang, F. Han, Self-assembled 3D hierarchical nanostructure of reduced GO nanosheets intercalated with CDs for high-rate supercapacitor electrodes, J. Alloys Compd. 727 (2017) 991–997. doi:10.1016/j.jallcom.2017.08.229.

[49] C. Liu, G. Han, Y. Chang, Y. Xiao, H. Zhou, G. Shi, High-performance supercapacitors based on the reduced graphene oxide hydrogels modified by trace amounts of

benzenediols, Chem. Eng. J. 328 (2017) 25–34. doi:10.1016/j.cej.2017.07.032.

[50] L. Chen, X. Zhang, H. Liang, M. Kong, Q. Guan, P. Chen, Z. Y. Wu, and S. H. Yu, Synthesis of Nitrogen-Doped Porous Carbon Nano fi bers as an E ffi cient Electrode Material for Supercapacitors, ACS Nano. (2012) 7092–7102. doi:10.1021/nn302147s.

[51] C. Tran, V. Kalra, Fabrication of porous carbon nanofibers with adjustable pore sizes as electrodes for supercapacitors, J. Power Sources. 235 (2013) 289–296. doi:10.1016/j.jpowsour.2013.01.080.

[52] T. Purkait, G. Singh, D. Kumar, M. Singh, R.S. Dey, High-performance flexible supercapacitors based on electrochemically tailored three-dimensional reduced graphene oxide networks, Sci. Rep. 8 (2018) 1–13. doi:10.1038/s41598-017-18593-3.